Short-range magnetic correlation, metamagnetism, and coincident dielectric anomaly in Na$_5$Co$_{15.5}$Te$_6$O$_{36}$

Rafikul Ali Saha [1,2,*], Jhuma Sannigrahi,[3] Ilaria Carlomagno,[4] S. D. Kaushik [5], Carlo Meneghini,[4] Mitsuru Itoh,[6] Vasudeva Siruguri [5], and Sugata Ray [1]

[1]*School of Materials Sciences, Indian Association for the Cultivation of Science, 2A & 2B Raja S. C. Mullick Road, Jadavpur, Kolkata 700 032, India*
[2]*Department of Microbial and Molecular Systems, Centre for Membrane Separations, Adsorption, Catalysis and Spectroscopy for Sustainable Solutions (cMACS), KU Leuven, Celestijnenlaan 200F, 3001 Leuven, Belgium*
[3]*School of Physical Sciences, Indian Institute of Technology Goa, Goa-403401, India*
[4]*Dipartimento di Scienze, Universitá Roma Tre, Via della Vasca Navale, 84 I-00146 Roma, Italy*
[5]*UGC-DAE-Consortium for Scientific Research Mumbai Centre, 246C 2nd floor Common Facility Building (CFB), Bhabha Atomic Research Centre, Mumbai 400085, India*
[6]*Materials and Structures Laboratory, Tokyo Institute of Technology, 4259 Nagatsuta, Yokohama 226-8503, Japan*

Here we explore the structural, magnetic, and dielectric properties of Na$_5$Co$_{15.5}$Te$_6$O$_{36}$, which reveal development of a short-range magnetic correlation and a dielectric anomaly in the system above Nèel temperature ($T_N=$) of 50 K. Low-temperature neutron powder diffraction (NPD) without any external magnetic field clearly indicates that the canted spin structure is responsible for the antiferromagnetic transition, and this canted spin structure brings several short-range ferromagnetic and antiferromagnetic correlations, and partially occupied Co form short-range magnetic correlation with other Co. Interestingly, a structural change in terms of changes in the lattice parameters and consequent development of dielectric anomaly around similar temperature is also recorded in the system. Additionally, the isothermal remanent magnetization and electron-spin resonance measurements reveal the presence of short-range magnetic correlations which coincide with an anomaly in the dielectric constant vs temperature curve. Further, a sharp jump in the magnetic-field-dependent magnetization clearly indicates the presence of metamagnetic transition, and magnetic-field-dependent NPD confirms that rotations of Co spins with applied magnetic field are responsible for this metamagnetic phase transition. Consequently, a magnetocaloric effect is developed in the system, which is suitable for the application in low-temperature refrigeration.

I. INTRODUCTION

Multiferroics has remained as one of the most important parts of condensed matter research for last few decades due to several possible technological applications [1,2]. There are several different ways to introduce multiple ferroic order in a system [3–19], with short-range magnetic correlation being one of them. There are a few compounds such as Ca$_3$Co$_2$O$_6$, Er$_2$BaNiO$_5$ which show displacive-type ferroelectricity involving off-centering of the magnetic ion due to short-range magnetic correlation [18,19]. Another langasite compound, Pb$_3$TeMn$_3$P$_2$O$_{14}$, shows covalency-driven local modulation of charge densities and development of ferroelectricity [4] while keeping global paramagnetism intact. In this context we probed the Na$_5$Co$_{15.5}$Te$_6$O$_{36}$ [20,21] (hexagonal space group $P6_3/m$) cobaltite system, where long-range interaction between Co ions is interrupted due to sporadic intervention by Na ions, as both the Na and Co ions share the same crystallographic site [Na(3)/Co(3)] (see Fig. 1(c) and Table I). Na$_5$Co$_{15.5}$Te$_6$O$_{36}$ contains two types of local coordinations of

single-valence Co (2+) (octahedra and trigonal prism), and the superexchange interaction pathways within edge-shared Co^{2+} octahedra are around 90°, while corner-connected Co-O-Co bond angles are around 120°, which signifies the presence of two types of magnetic interactions. Co-based compounds often offer interesting properties due to the possible existence of different Co-oxidation states (+2, +3, and +4), with several local coordinations (tetrahedra, octahedra, trigonal prism, and so on) around Co and most importantly, various spin states within the same Co valence [19,22,23]. Zhao *et al.* [21] has reported the magnetic ground-state and field-induced transitions of an $S = 1/2$ Ising antiferromagnet (AFM) with a stacked kagome geometry of Na$_5$Co$_{15.5}$Te$_6$O$_{36}$ and two successive transitions below the long-range AFM transition. But there is no direct evidence of spin structure for long-range AFM transition as well as magnetic-field-induced transitions. Furthermore, the magnetic properties and dielectric properties above the long-range AFM transition were not discussed. Therefore it would be interesting to know the exact spin structure and dielectric properties of this system.

In this report we discuss the crystal structure, magnetic structure, and dielectric properties of Na$_5$Co$_{15.5}$Te$_6$O$_{36}$. A low-temperature magnetic structure study, using neutron

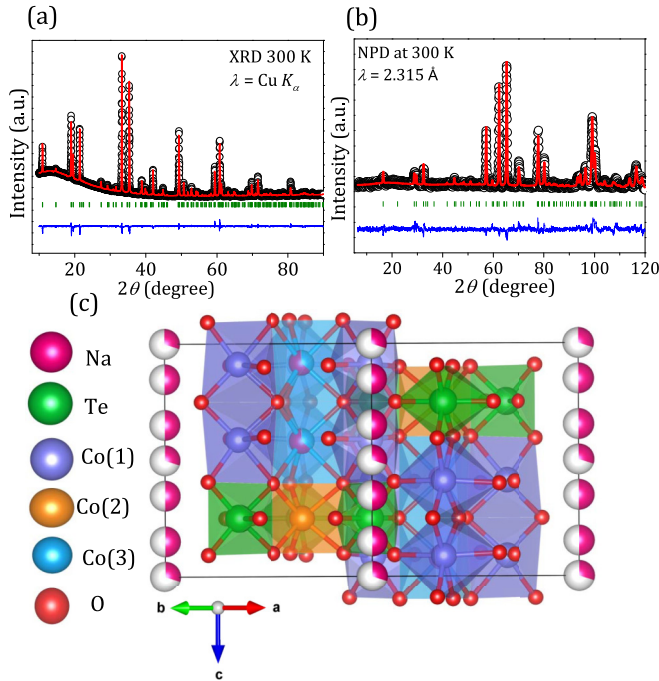*rafikulalisaha@gmail.com, rafikulali.saha@kuleuven.be

FIG. 1. (a), (b) Rietveld refined XRD and NPD of NCTO at room temperature, respectively. Black open circles represent the experimental data, and red line represents the calculated pattern. The blue line represents the difference between the observed and calculated pattern, and green lines signify the position of Bragg peaks. (c) Refined crystal structure of NCTO. White/pink sites are partially occupied Na(1) and Na(2) sites.

TABLE I. The sample NCTO is refined within a single crystallographic phase using a hexagonal space group $P6_3/m$. Lattice parameters of NCTO: $a = b = 9.3231(9)$ Å, $c = 9.0682(7)$ Å, $\alpha = \beta = 90°$, $\gamma = 120°$. $R_{wp} = 14.51$, $R_{exp} = 8.16$, $\chi^2 = 3.16$.

Atom	Site	x(Å)	y(Å)	z(Å)	B_{iso}	Occupancy
Te	6h	0.6560(9)	0.0098(5)	0.0000	0.142(8)	1.0
Co(1)	12i	0.3438(1)	0.9934(5)	0.0877(9)	0.213(5)	1.0
Co(2)	2d	0.66667	0.33333	0.2500	0.213(5)	1.0
Na(1)	2b	0.0000	0.0000	0.0000	0.258(4)	0.3
Na(2)	4e	0.0000	0.0000	0.6520(6)	0.258(4)	0.5
Co(3)	4f	0.33333	0.66667	0.0818(3)	0.213(5)	0.37
Na(3)	4f	0.33333	0.66667	0.0818(3)	0.213(5)	0.63
O(1)	12i	0.6904(4)	0.8883(8)	0.0908(6)	0.174(3)	1.0
O(2)	12i	0.6097(7)	0.1400(2)	0.1007(4)	0.174(3)	1.0
O(3)	6h	0.8805(1)	0.1732(6)	0.2500	0.174(3)	1.0
O(4)	6h	0.4132(8)	0.8627(3)	0.2500	0.174(3)	1.0

99.99%). The mixture was initially calcined at 600 °C in air for 12 h. The resultant mixture was then reground and finally annealed at 800 °C for 12 h in air. The phase purity of the sample was checked through x-ray powder diffraction (XRD) measured with a Bruker AXS: D8 Advanced x-ray diffractometer equipped with Cu $K\alpha$ radiation. Temperature-dependent XRD was carried out on a Rigaku Smartlab (9 kW) XG equipped with Cu $K\alpha$ to probe the temperature-dependent structural phase transitions. The obtained XRD data were analyzed using the Rietveld technique, and refinements of the crystal structure were performed by the FULLPROF program [24]. The x-ray photoemission spectroscopy (XPS) measurements were carried out using an Omicron electron spectrometer equipped with a Scienta omicron Sphera analyzer and Al $K\alpha$ monochromatic source with an energy resolution of 0.5 eV. XPS data were fitted using KOLXPD software. Neutron powder diffraction measurements were carried out on powder samples using the multiposition-sensitive detector-based focusing crystal diffractometer set up by UGC-DAE Consortium for Scientific Research Mumbai Centre at the National Facility for Neutron Beam Research (NFNBR), Dhruva reactor, Mumbai (India). NPD at room temperature and 3 K have been taken using a wavelength of 2.315 Å, while field-dependent NPD at 10 K have been performed using a wavelength of 1.48 Å. The NPD data were analyzed via refinement using the JANA2006 program [25]. Co K-edge x-ray absorption fine-structure (XAFS) spectra were collected at the XAFS beamline of the Elettra Synchrotron Centre, Italy [26]. The dc magnetic measurements were carried out using a superconducting quantum interference device (SQUID) magnetometer (Quantum Design, USA) over a temperature range of 2–300 K in magnetic fields up to ±7 Tesla and also in a vibrating-sample magnetometer (Cryogenic, UK). For calculation of the magnetocaloric effect, virgin curves of magnetic-field-dependent magnetization ($M - H$) up to 16 T have been taken using a vibrating-sample magnetometer (VSM) in a cryogenic physical property measurement system (PPMS). The heat capacity was measured by relaxation method in a quantum design physical property measurement system (PPMS). The permittivities were measured using a Hewlett-Packard Precision LCR meter (HP4284A) at an ac

powder diffraction (NPD), reveals the presence of canted antiferromagnetic ordering. In addition to the antiferromagnetic transition (T_N), the dc magnetic susceptibility measurements further suggest the presence of a short-range ferromagnetic correlation above T_N, while an anomaly is observed at the same temperature in temperature-dependent dielectric data as well as in lattice parameter variation plots, indicating the presence of a possible magnetoelectric coupling in the system. Further electron-spin resonance and isothermal remanent magnetization measurement support the presence of short-range magnetic correlation above the Néel temperature (50 K). The system also exhibits a metamagnetic transition in magnetic-field-dependent isothermal magnetization measurement, inducing a magnetocaloric effect in the system, which is suitable for applications in low-temperature refrigeration. The metamagnetic transition has been probed through magnetic-field-dependent NPD, which confirms that rotations of Co spins with applied magnetic field are responsible for this transition.

II. METHODOLOGY

A. Experimental techniques

Polycrystalline $Na_5Co_{15.5}Te_6O_{36}$ (NCTO) was prepared using a conventional solid-state reaction technique. The NCTO sample was synthesized by taking stoichiometric amounts of high-purity Na_2CO_3 (Merck⩾99.5%), TeO_2 (Sigma-Aldrich 99.9995%), and Co_3O_4 (Sigma-Aldrich

TABLE II. Bond valence sum calculation.

Element	Bond length (Å)	Valency
Co(1)	2*Co(1)-O(1) - 2.05	1.9
	2*Co(1)-O(2) - 2.24	
	Co(1)-O(3) - 2.07	
	Co(1)-O(4) - 2.18	
Co(2)	6*Co(2)-O(2) - 2.14	1.8
Co(3)	3*Co(3)-O(2) - 2.34	1.2
	3*Co(3)-O(4) - 2.24	
Na(3)	3*Na(3)-O(2) - 2.34	1.1
	3*Na(3)-O(4) - 2.24	
Te	2*Te-O(1) - 1.91	5.8
	2*Te-O(2) - 1.97	
	Te-O(3) - 1.90	
	Te-O(4) - 1.95	

FIG. 2. (a) Normalized Co K-edge x-ray absorption near-edge spectra of NCTO (red curve), CoO(OH) (blue curve), and CoO (green curve). Inset shows the first-order derivative of normalized data. XPS spectra of (b) Na $1s$, (c)Te $3d$, and (d) O $1s$. Black open circles and red lines are the experimental and fitted data. respectively. Green and violet line are the two singlets for O $1s$.

level of 1 V mm^{-1}. A cryogenic temperature system (Niki Glass LTS-250-TL-4W) was used to control the temperature within the range of 4–350 K. The dielectric hysteresis loops were measured using a ferroelectric measurement system (Toyo Corporation FCE-3) equipped with an Iwatsu ST-3541 capacitive displacement meter having a linearity of 0.1% and a resolution of 0.3 nm. X-band electron paramagnetic resonance (EPR) measurements were performed on a Jeol JES-200 spectrometer.

III. RESULTS AND DISCUSSION

A. Structural and electronic characterization

Powder x-ray diffraction (XRD) data of NCTO at 300 K confirms phase purity, and the structural refinement has been performed by considering the earlier reported [20,21] hexagonal space group $P6_3/m$ (space group no. 176), as shown in Fig. 1(a) and Table I. Temperature-dependent x-ray diffractions of NCTO compound have been performed over a wide temperature range of 5–300 K. The Rietveld refinements of these collected XRD patterns have been done using the same space group $P6_3/m$. Further, room-temperature neutron powder diffraction experiments on the sample were performed to get the exact position and occupancy of lighter oxygen atoms, as shown in Fig. 1(b). Refinement of the NPD data at room temperature revealed very similar parameters as obtained from the analysis of the XRD pattern. The crystal structure of NCTO contains one formula per unit-cell, depicted in Fig. 1(c). Here, both Te and Co are coordinated by six oxygen ions, but the geometry of their polyhedra are different. Te and Co(1) form a slightly distorted octahedra, while two Co [Co(2) and Co(3)] make distorted trigonal prisms. Both room-temperature XRD and NPD reveal the presence of a rare disorder between Co(3) and Na(3), where Co(3) and Na(3) reside on the same site with partial occupancy as 0.37 and 0.63, respectively. The coordination polyhedra around the Co(3)/Na(3) site is on average larger than those around the Co(1,2) sites due to the larger Na$^+$ ionic radius (Table II). Two nearest-neighbor Co(3)/Na(3) distorted trigonal prisms are connected via common face sharing, while they are attached
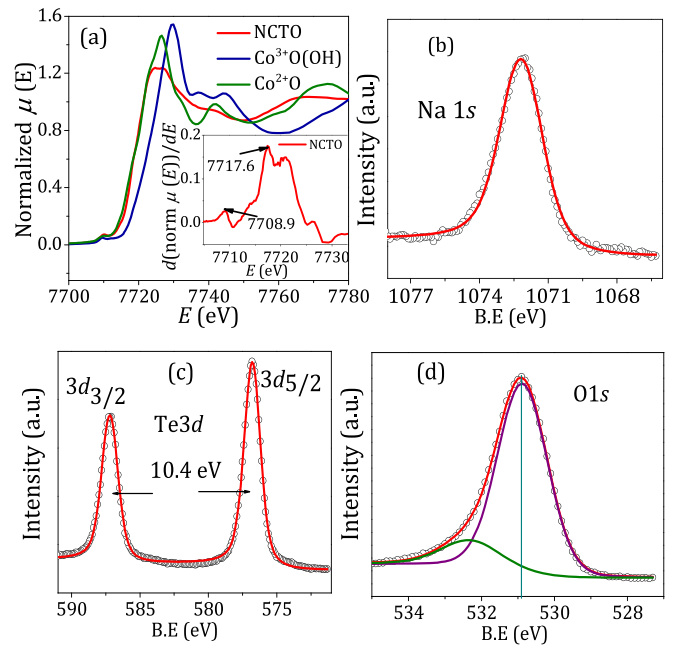
with a Co(1) octahedra and Co(2) trigonal prism via edge sharing and common face sharing, respectively. On the other hand, two Co(1) octahedra are connected via edge sharing and one Co(1) octahedra is connected with Co(2) trigonal prism via corner sharing.

In order to maintain the charge neutrality of the sample, the oxidation states of Na, Co, and Te are expected to be 1+, 2+, and 6+, respectively. However, to know the actual valence states of the cation bond valence sum calculation (BVS) the formula $V = \sum \exp[(R_0 - R_i)/b]$ is used, where V is the valence state of a cation, R_i is the observed bond length, R_0 is the tabulated parameter expressing the ideal bond length when the element i has exactly valence 1 and b is an empirical constant, typically 0.37 Å, shown in Table II. Te, Co(1), and Co(2) show 5.8, 1.9, and 1.8 oxidation states, respectively, but surprisingly, partially occupied Co(3) [with Na(3)] shows a positive charge of only 1.2, which is much smaller than the usual 2+, while a 1.1 valency for Na is shown. Therefore, in order to accommodate Co(3) at the Na(3) site, the Co-O bond length should be changed and consequently, a distortion would be developed in the Co(3) containing trigonal prism polyhedra.

As Co always has the tendency to be in a variety of charge states as well as spin states in oxides [27–29], precise estimation of the Co oxidation state in the present compound is of central importance in the context of Co-mediated physical properties. Therefore, to know the true valency of Co, Co K-edge x-ray absorption near-edge spectroscopy (XANES) was carried out and presented in Fig. 2(a). Consequently, the first-order derivative of the normalized XANES spectrum [see inset to Fig. 2(a)] identifies a pre-edge peak at 7708.9 eV

(due to 1*s* to 3*d* transition caused by 3*d*-4*p* mixing [30,31]) and an absorption edge peak at 7717.6 eV (due to transition Co 1*s* orbital to molecular orbital with Co 4*p* [30,31]). We have compared the XANES of the experimental data (NCTO sample) with those from CoO (being Co^{2+}) and CoO(OH) (being completely Co^{3+}), as shown in Fig. 2(a). The raising of the edge on the data perfectly matches with the Co^{2+} state [see Fig. 2(a)], which confirms the 2+ oxidation state of Co in the sample [32–34].

Further XPS measurements were carried out to confirm the oxidation states of the constituent elements of this compound. The core-level Na 1*s*, Te 3*d*, and O 1*s* spectra, along with the fitting curves shown in Figs. 2(b)–2(d), clearly indicate the respective charge states. The energy position of the Na 1*s* (1072.1 eV) reveals the expected 1+ charge state [35], while the peak positions of Te 3*d* doublets (576.8 eV, 587.2 eV) along with their energy separation (10.4 eV) suggest a 6+ valence state of Te in NCTO [36]. The O 1*s* spectrum of NCTO has been fitted by considering two singlets [see the green and violet lines of Fig. 2(d)], which signifies the presence of multiple oxygen sites in this compound [37].

B. Magnetic, thermodynamic, and dielectric characterization

Thermal variations of magnetic susceptibility (χ) have been measured under the applied magnetic field of $H = 100$ and 500 Oe in the zero-field-cooled cooling (ZFC), field-cool cooling (FCC), and field-cool heating (FCH) conditions. As displayed in Figs. 3(a), 3(b) and Fig. S1 of the Supplemental Material [38], three different types of magnetic transitions [a clear antiferromagnetic (AFM) transition (T_N) around 50 K, a weak shoulderlike anomaly at around 45 K, and a bifurcation between ZFC and FC below 40 K] are identified in the ZFC and FC curves, which are consistent with the previous study [20,21]. These features in magnetic susceptibility are further characterized by the zero-field heat capacity measurements (C_p vs T). A sharp λ-like anomaly at around 50 K is an authentication mark of a thermodynamic phase transition into a long-range magnetic ordering in the C_p vs T data [see Fig. S2(a) of Supplemental Material [38]]. The temperature-dependent zero-field C_p above 90 K has been fitted using the Debye-Einstein model (see Fig. S2(b) of Supplemental Material [38]) and gives the Debye temperature ($\theta_D = 300$ K), two Einstein temperatures, $\theta_{E1} = 250$ K and $\theta_{E2} = 824.8$ K. The magnetic specific heat is then extracted after subtracting the lattice contribution from the total C_p. The magnetic entropy of the system was subsequently calculated by using the formula $S_m(T) = \int C_{mag}/T \, dT$, and the results are displayed in Fig. S2(b) of the Supplemental Material [38]. The magnetic entropy release is 8.5 J/mol Co K^2 above 75 K, which is about 73.9% of the expected R*ln(2S + 1), with $S = 3/2$ of the d^7 Co^{2+} ion for a complete magnetic ordering. Therefore the retention of magnetic entropy (26%) further supports the high competition between ferromagnetic and antiferromagnetic interactions and/or frustrated nature of the Co spins in this system [39]. Further, the Curie-Weiss (C-W) fit [$\chi = \chi_0 + C/(T - \theta_{CW})$, where χ_0 is the temperature-independent paramagnetic susceptibility, C is the Curie constant related to the effective moment, and θ_{CW} is the Weiss temperature] of the 100-Oe field-cooled heating susceptibility data in the
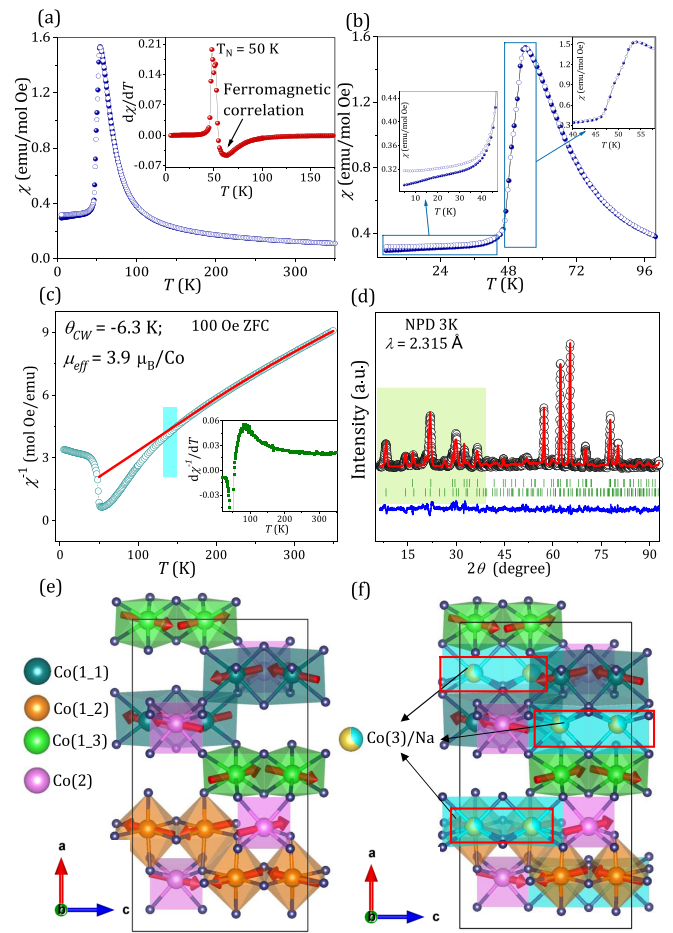

FIG. 3. (a) ZFC and FCH of NCTO at $H = 100$ Oe. Inset shows the first-order derivative of $\chi(T)$. (b) Expanded portion of ZFC and FC curve at ZFC and FC, where one can clearly see shoulderlike behavior and bifurcation between ZFC and FC. (c) Inverse susceptibility data at 100 Oe. Open circle data and red line are experimental and Curie-Weiss fitted data, respectively. Inset shows the first-order derivative of $\chi^{-1}(T)$. (d) Rietveld refined NPD of NCTO at 3 K. Black open circles represent the experimental data, and red line represents the calculated pattern. The blue line represents the difference between the observed and calculated pattern, and green lines signify the position of Bragg peaks. (e) Refined magnetic structure of NCTO. All Co polyhedra connections with spin structure which are responsible for long-range ordering. (f) Partially occupied Co polyhedra and spin structure of fully occupied Co. Red squares are the positions of partially occupied Co [Co(3)/Na].

temperature range of $T = 180$–350 K gives a negative Weiss temperature ($\theta_{CW} = -6.3$ K), which indicates antiferromagnetic interactions between the neighboring Co spins. The effective paramagnetic moment $\mu_{eff} = 3.9 \, \mu_B/Co$, obtained from the C-W analysis, correlates quite well with the theoretical value of 3.87 μ_B/Co for high spin Co^{2+}. Interestingly, the C-W fit deviates from the experimental $1/\chi(T)$ versus T curve in the form a sharp downturn from around much higher temperature of 155 K [see Fig. 3(c)], which is further supported by the respective first-order derivative curve [see inset of Fig. 3(c)]. Such a signature is usually attributed to the Griffiths phase singularity [40,41], where short-range

FM clusters [42] appear upon cooling, or equivalently, finite spin-canted clusters exist because of a strong basal-plane anisotropy in microscopically phase-separated regions much above the bulk T_N [43]. A prominent dip in the first temperature derivative of magnetic susceptibility data [see inset of Fig. 3(a)] also supports the presence of ferromagnetlike interaction above Nèel temperature.

In order to further clarify the magnetic ground state of NCTO, we have conducted neutron powder diffraction (NPD) experiments at room temperature and below long-range ordering temperature (at 3 K), which are shown in Figs. 1(b) and 3(d), respectively. Low-temperature NPD pattern reveals additional Bragg peaks (forbidden in the structural space group) as well as an increase in the intensity of some of the nuclear peaks [see the green shaded region of Fig. 3(d)]. The additional intensities are observed only at a lower 2-theta region pointing to their magnetic origin. All the magnetic reflections can be indexed using the $k = (0.5, 0.5, 0)$ propagation vector. The magnetic structure has been refined using JANA2006 software considering the Shubnikov magnetic space group $P[B]21/m$, with the origin shifted by $(1/4, 0, 1/4)$. We have performed the magnetic structure refinement without considering long-range ordering of the partially occupied Co(3) site (Co/Na = 0.37/0.63), because the Co(3) moments share the same site with Na, and the random presence of Na at the Co(3) site would expect to hinder the Co(3) ions from participating in the long-range magnetic interactions with the other neighboring Co sites. Within this assumption we get a reliable fitting, which shows a canted AFM structure, where the spins of fully occupied Co(1-1), Co(1-2), Co(1-3), and Co(2) are aligned along c axis but canted towards the a-b plane [see Fig. 3(e)]. Magnetic moment per Co site ($\mu_{\mathrm{eff}} = 3.7\,\mu_B/\mathrm{Co}$), obtained from neutron refinement, is consistent with the spin-only moment of Co^{2+} for the high-spin configuration ($3.87\,\mu_B/\mathrm{Co}$). Refinement of 3-K data shows that Co spins within the edge-shared Co motifs (two orange and green octahedra) are directed along the c axis but canted within the a-b plane, as depicted in Fig. 3(e). These connectivities satisfy the Co-O-Co bond angle $\sim 85° \sim 96°$ of the superexchange pathways. On the other hand, spins belonging to the 1D zigzag chains of the corner-shared CoO$_6$ octahedra [see orange and green octahedra in Fig. 3(e)] with the Co-O-Co bond angle of $123.5°$ cause mutually opposite canted spin alignment. The CoO$_6$ triangular prisms [pink polyhedra in Fig. 3(e)] also share their corners with the neighboring Co motifs, creating bond angles of $106.1°$ and $155.7°$. From the low-temperature zero-field NPD we also confirm that canted spin structure is responsible for the long-range AFM ordering at 50 K, and this canted spin structure brings several short-range ferromagnetic and antiferromagnetic correlations (see Fig. S3 of the Supplemental Material [38]). However, another interesting feature appears when partially occupied Co(3) is introduced in the spin structure, as shown in Fig. 3(e). Partial occupancy between Co(3) and Na signifies that Co(3) is distributed inhomogeneously in the unit cell. As a result, where Co(3) is present in the unit cell, it is connected via face sharing with the Co(2) trigonal prism, edge sharing with Co(1-1), Co(1-2), and Co(1-3), as shown in Fig. 3(f). The downward deviation from C-W law in the inverse susceptibility data, indicating the presence of
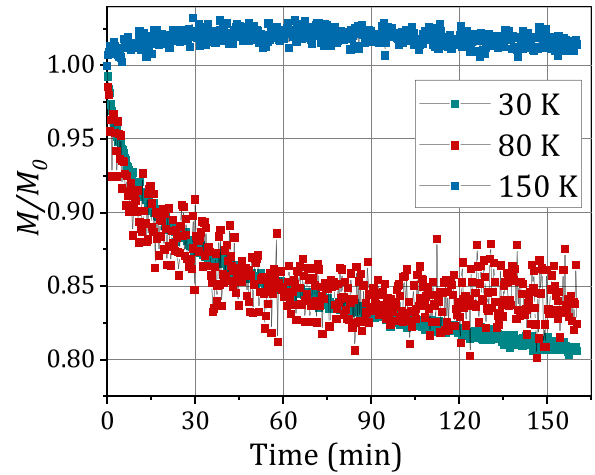

FIG. 4. Isothermal remanent magnetization at three different temperatures: 30 K, 80 K, and 150 K.

short-range magnetic correlation, may therefore be attributed to the magnetic interactions of partially occupied Co(3) with other neighboring Co ions.

The downward deviation from C-W law in the inverse susceptibility data indicates the presence of short-range magnetic correlation. Furthermore, to probe the existence of the short-range magnetic correlations we have measured isothermal remanent magnetization (IRM) at three different temperatures (150 K, 80 K, and 30 K), as shown in Fig. 4. We noticed no magnetic relaxation at 150 K, but there are clear relaxations at 80-K and 30-K IRM data. It is evident that the M_{IRM} (M/M_0) undergoes a slow decay with time, which is a signature of magnetic materials having different magnetic interactions, hysteretic magnetization, and/or glassy dynamics [44–47]. Our electron paramagnetic resonance (EPR) measurement at 300 K and liquid nitrogen temperature (illustrated in the Supplemental Material [38], and see also Refs. [42,48–51], which have been used in the Supplemental Material) confirmed the existence of ferromagnetic clusters in the system.

Both cooling and heating cycles of the temperature dependence of the dielectric constant ($\varepsilon'/\varepsilon_0$) and dielectric loss ($\tan\delta$) of NCTO at frequencies from 0.1 kHz–1000 kHz in the temperature range of 2–300 K are shown in Figs. 5(a) and 5(b), respectively. For the lowest frequency data we can see that an anomaly in both temperature-dependent dielectric constant and loss ($\tan\delta$) data starts to develop from 72 K, which shifts to higher temperature with increasing frequencies, implying a thermally activated relaxation process. Observation of dielectric anomaly/property could be intrinsic or extrinsic in origin. In general, the colossal dielectric constants are mostly based on Maxwell-Wagner-type extrinsic effects (effect of grain boundaries). The natural explanation of apparent colossal dielectric constant is contact effects, and in ceramic samples the effects due to grain boundary may play a similar role and hence cause further enhancement of the dielectric constant. At these interfaces (metal to-insulator contacts, intergrain boundaries) depletion layers are generated, which yield Maxwell-Wagner-type relaxations when measured by standard dielectric techniques with metallic electrodes and two-point contact configurations. However,
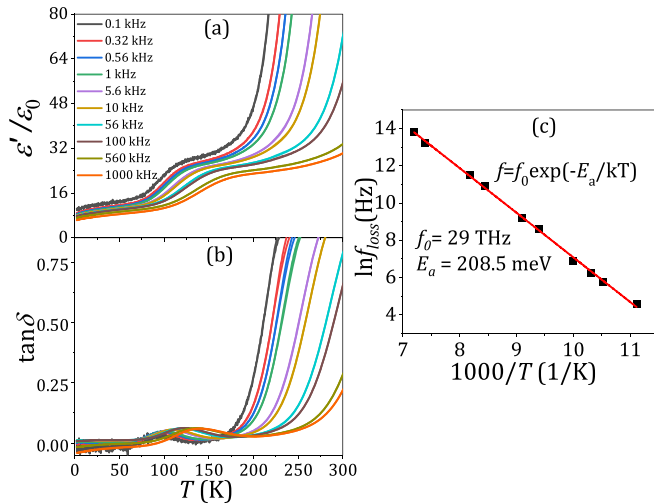
FIG. 5. (a), (b) Temperature dependence of real part of dielectric constant $\varepsilon'/\varepsilon_0$ and $\tan \delta$ loss data of NCTO at different frequencies. (c) Fitting of the activation energy corresponding to the dielectric loss.

the dielectric properties of a material are often strongly influenced by its crystal structure and the way in which the atoms or ions are arranged. Any changes in the crystal structure can lead to alterations in the electronic and/or ionic polarizability, which in turn affects the dielectric behavior of the material. In some cases, the dielectric anomaly itself can be a result of a structural phase transition, which involves a change in the symmetry of the crystal lattice. This type of transition is often accompanied by a sudden change in the dielectric constant, which can be detected as a sharp peak in the temperature or frequency dependence of the dielectric response. On the other hand, structural distortions can also arise due to the interaction between the lattice and other degrees of freedom, such as magnetic, electronic, or lattice vibrations. These distortions can give rise to changes in the dielectric response, which can manifest as anomalies in the dielectric constant or loss. In case of the NCTO sample, as the peak position of the dielectric anomaly changes with frequency, we identified the f_{loss} and corresponding temperature (T), and plotted as $\ln f_{\text{loss}}$ versus $1000/T$, where f_{loss} is the frequency corresponding to the peak of the loss ($\tan\delta$) curves at the corresponding temperature T, as shown in Fig. 5(c). The relaxation shows linear behavior which can be fitted to the Arrhenius law $f = f_0 \exp(E_a/k_B T)$, where E_a is the activation energy, f_0 is the pre-exponential factor, and k_B is the Boltzmann constant, and the fitting reveals the thermal activation energy (E_a) of relaxation to be 208 meV. However, the dielectric anomaly exists only in the range of 63–150 K (illustrated in the Supplemental Material [38]). Apart from the temperature-dependent dielectric measurements, we have measured electric polarization with varying electric field ($P - E$ loops) at three different temperatures (300 K, 160 K, and liquid nitrogen temperature), as shown in Fig. S6 of the Supplemental Material [38], which shows that the $P - E$ loop at 160 K and above is a bananalike curve. The $P - E$ loop at or above 160 K does not exhibit any saturation, even at high electric fields, suggesting leaky-type materials which do not possess perfect insulation properties

and exhibit a certain amount of electrical conductivity [52]. The $P - E$ loop at liquid nitrogen temperature shows clear saturation at around ± 100 kV/cm, indicating the presence of spontaneous polarization that can be reversed by an external electric field. In short, the extrapolation of the Arrhenius-fitted data and the measured $P - E$ loops at three different temperatures strongly affirm the dielectric anomaly and spontaneous polarization in the 63–150 K range. Therefore, in our case we can affirm that the appearance of the dielectric anomaly within this temperature range is an intrinsic property of the material, which is very common for the relaxor ferroelectric materials [53,54]. Relaxor ferroelectrics are typically complex solid solutions, where different ions occupy the same crystallographic site and cause local disorder that gives rise to the relaxor behavior. In our particular case, we hypothesize the presence of relaxor ferroelectrics where some local distortion causes the development of spontaneous polarizations. But above this temperature range, the increasing values of the dielectric constant and loss could come due to contact effects, which is common for ceramic samples [55].

Further, we measured temperature-dependent XRD (temperature range 300–5 K), which has been shown in Fig. S7(a) of the Supplemental Material [38]. An unusual behavior in the Bragg peak positions with temperature in a certain temperature range has been observed, as shown in Figs. S7(b) and S7(d) of the Supplemental Material [38]. In addition, we also observed a gradual decrease in the peak intensity [at around 10.7°, see Fig. S7(c)] with decreasing temperature until around 150 K, and below 150 K it remains constant. Further, from the Rietveld refinement of all temperature-dependent XRD data, we got different slopes in two different temperature regions as well as small anomalies or scattered data points at the junction point of two slopes in thermal variations of refined lattice parameters a, b, c and volume of the unit cell (V), which coincide with temperature dependence of the dielectric anomaly, as shown in Figs. 6(a) and 6(c), signifying the correlation between structural distortion and dielectric anomaly. Due to rather tiny changes in position coordinates across the phase transition, the present Rietveld refinements could not conclusively determine the true symmetry of the low-temperature phase. Such difficulties are not unusual when the lattice distortions are weak [18,56]. Furthermore, we track the movement of the atomic position of the Co(3) with temperature, as shown in Fig. S8 of the Supplemental Material [38]. As the x and y coordinates are fixed for the position of Co(3) atom (1/3, 2/3, z), we plot the variation of the z coordinate with temperature (see Fig. S8), which clearly shows a sudden drop below 150 K ($\sim 10\%$), thus indicating that above 150 K there is almost negligible shift of Co(3), while below 150 K there is a noticeable shift in Co(3) atom towards the negative c direction. Therefore we can conclude that the relative movement of the magnetic element is responsible for the structural deformation and consequently creating local dipole moments. However, it is interesting to note that below 150 K the compound goes to another structural symmetry, which matches with the dielectric anomaly and a downturn deviation in the inverse susceptibility temperature region [see Figs. 6(a)–6(c)]. Further, we study the temperature-dependent dielectric constant under 9-Tesla magnetic field and zero field and plot the difference
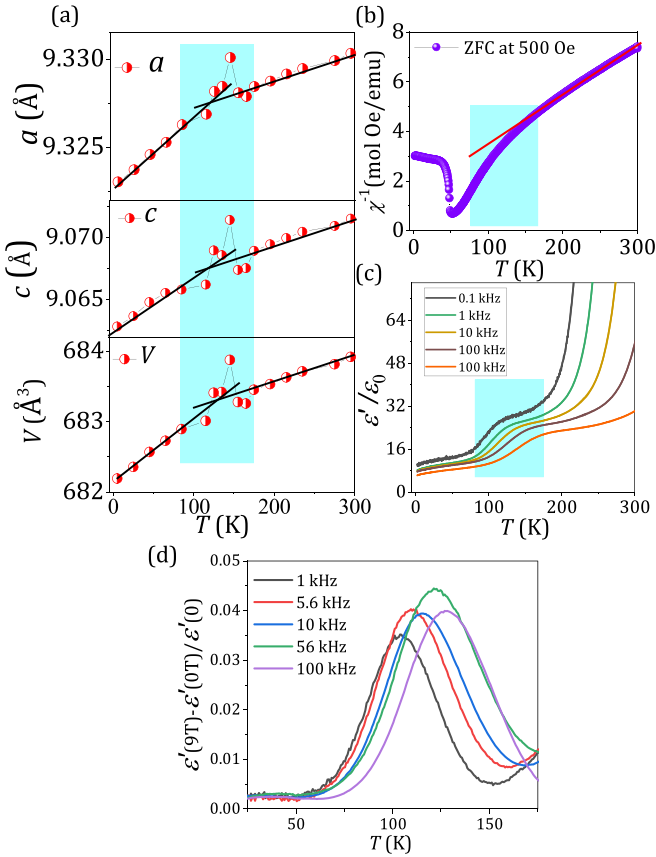
FIG. 6. (a)–(c) Temperature dependence of lattice parameters, unit-cell volume, and inverse susceptibility data, and thermal variation of real part of dielectric constant $\varepsilon'/\varepsilon_0$, respectively. (c) Difference between the thermal variation of real part of dielectric constant at applied magnetic field 9 T and zero field.

([ε'(9T)-ε'(0T)]/ε'(0T) vs T), as shown in Fig. 6(d). A significant change is observed between the with-field ($H = 9$T) and without-field data, as indicated in Fig. 6(d), signifying the presence of magnetoelectric coupling in the system. As a result, we can conclude that structural distortion is related to the dielectric anomaly. Therefore we may comment that short-range magnetic correlations develop among the Co(3) spins above long-range AFM, which is simultaneously related to Co(3) off-centering, dielectric anomaly, and development of spontaneous electric polarization at the same temperature range.

C. Field-induced changes in magnetic response

Further, we have measured isothermal magnetization data $M(H)$ at different temperatures (2, 10, 30, and 55 K), as shown in Fig. 7(a). The $M(H)$ curve at 2 K exhibits a high coercive field ($H_C = 25$ kOe) nonsaturating behavior up to 7 Tesla, indicating the presence of high magnetocrystalline anisotropy within the predominantly antiferromagnetic environment. Surprisingly, a sudden jump at around 26.5 kOe of applied field in the 10-K $M(H)$ data signifies the presence of metamagnetic phase transition. The signature of metamagnetism is also present at 30 K $M(H)$ data but at slightly lower magnetic field [see Fig. 7(a)]. Additionally, this

compound shows almost ∼9% magnetocaloric effect (MCE) at an applied magnetic field of 16 Tesla (detailed calculation is given in the Supplemental Material [38]).

Furthermore, we have carried out the neutron powder diffraction under magnetic fields $\mu_0 H = 0$ Tesla and 3 Tesla at 10 K to ascertain the modification in spin structure beyond the metamagnetic phase transition. Neutron powder diffraction experiments at 3 K and 10 K have been performed using wavelengths of 2.315 Å and 1.48 Å, respectively.

NPD at 10 K for zero and 3 Tesla applied magnetic field collected at 1.48 Å are presented in Figs. 7(b) and 7(c). Clear differences are observed in the NPD diffraction pattern with increasing magnetic field pointing towards distinct changes in the magnetic unit cell as well as spin structure with applied magnetic field. In order to unfold the origin of all the observed field-induced subtle changes in the NPD data, we have first fitted the zero-field data of 10 K using the propagation vector [0.5, 0.5, 0] and the Shubnikov magnetic space group $P[B]2_1/m$, with the origin shifted by (1/4, 0, 1/4), which gave the similar kind of spin structure to the zero-field 3-K data. Interestingly, attempts to fit the 3-T data using the same propagation vector [0.5, 0.5, 0] as zero field failed to capture all the extra peaks generated under the externally applied magnetic fields. On the other hand, systematic changes in the recorded magnetic peak intensities with increasing applied magnetic field could quite well be captured by assuming the [0, 0, 0] propagation vector. The magnetic structures of the 3-Tesla data have been refined considering the Shubnikov magnetic space group $P6_3'/m$, as shown in Fig. 7(c), and got quite satisfactory fitting. Consequently, the magnetic unit cell and the respective spin structures (obtained from the refinement) for zero- and 3-Tesla applied magnetic field are illustrated in Figs. 7(d) and 7(e). The depicted field-induced changes in the spin structures [see Figs. 7(d) and 7(e)] clearly demonstrate that the spin-flop transition mechanism upon applied magnetic fields is responsible for the observed metamagnetic transition observed in the $M(H)$ curve [see Fig. 7(a)]. It should be noted that the refined values of the Co magnetic moments remain very similar and consistent at the zero field (3.8 μ_B) and 3-Tesla field (3.9 μ_B), respectively.

IV. CONCLUSION

We have reported the results of detailed structural, magnetic, and dielectric studies of a complex oxide system, Na$_5$Co$_{15.5}$Te$_6$O$_{36}$. XRD and NPD measurements revealed that among the Co polyhedra, partially occupied Co(3) becomes larger due to the greater ionic radius of Na$^+$. According to BVS calculation, this polyhedra does not satisfy the valency of 2+. Therefore, to maintain the proper oxidation state of Co, the local symmetry of the Co(3) polyhedra is modified. From the zero-field neutron powder diffraction we also confirm that canted spin structure is responsible for the long-range antiferromagnetic ordering, and this canted spin structure brings several short-range ferromagnetic and antiferromagnetic correlations, and additionally, we can say that partially occupied Co at the Co(3) site locally creates magnetic islands in the system which help to change the polyhedra of that particular Co. Isothermal remanent magnetization and EPR data also confirmed the presence of such short-range magnetic
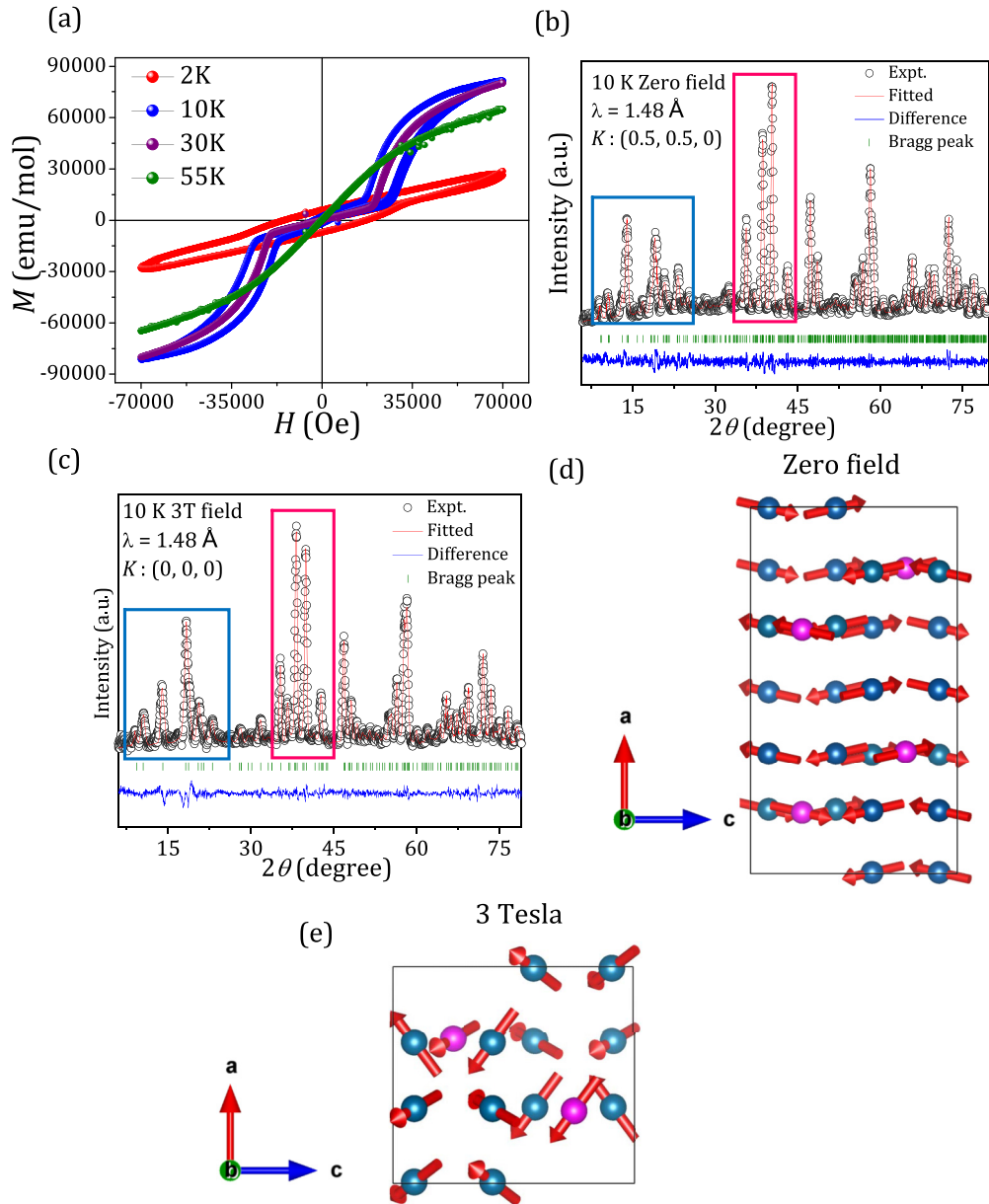
FIG. 7. (a) M vs H data at 2, 10, 30, and 55 K. (b), (c) Refined neutron powder diffraction pattern in magnetic field $\mu_0 H = 0$ and 3 T at 10 K, respectively. Black open circles represent the experimental data, and red line represents the calculated pattern. The blue line represents the difference between the observed and calculated pattern, and green lines signify the position of Bragg and magnetic peaks. (d), (e) Magnetic structure of NCTO compound in different magnetic field $\mu_0 H = 0$ and 3 T, respectively. Dark cyan and pink spheres are Co(1) and Co(2), respectively.

correlation above the Néel temperature. The anomaly due to short-range magnetic correlation coincides with slope change in the temperature-dependent lattice parameter as well as dielectric anomaly and development of spontaneous electric polarization. Finally, a significant change between the with-field ($H = 9$T) and without-field data above long-range AFM ordering signifies the presence of a possible magnetoelectric coupling in the system. As a result, we may state that the appearance of magnetoelectric coupling in this compound arises from the local off-centering of Co(3) centers, caused due to the short-range magnetic correlations among the Co(3) spins. In addition, isothermal magnetization as well as magnetic-field-dependent NPD, clearly affirm that spin-flop transition

with increasing magnetic field causes metamagnetic phase transition. Hence, our results introduce another possible short-range magnetic-correlation-driven multiferroic system as well as a spin-flop metamagnetic candidate.

[1] T. Kimura, T. Goto, H. Shintani, K. Ishizaka, T. Arima, and Y. Tokura, Nature (London) **426**, 55 (2003).

[2] N. A. Spaldin and M. Fiebig, Science **309**, 391 (2005).

[3] X. He and K. J. Jin, Phys. Rev. B **94**, 224107 (2016).

[4] R. A. Saha, A. Halder, T. Saha-Dasgupta, D. Fu, M. Itoh, and S. Ray, Phys. Rev. B **101**, 180406(R) (2020).

[5] N. A. Hill and K. M. Rabe, Phys. Rev. B **59**, 8759 (1999).

[6] L. M. Volkova and D. V. Marinin, J. Supercond. Novel Magn. **24**, 2161 (2011).

[7] K. C. Pitike, W. D. Parker, L. Louis, and S. M. Nakhmanson, Phys. Rev. B **91**, 035112 (2015).

[8] R. Seshadri and N. A. Hill, Chem. Mater. **13**, 2892 (2001).

[9] D. V. Efremov, J. van den Brink, and D. I. Khomskii, Nat. Mater. **3**, 853 (2004).

[10] S. W. Cheong and M. V. Mostovoy, Nat. Mater. **6**, 13 (2007).

[11] N. Hur, S. Park, P. A. Sharma, J. S. Ahn, S. Guha, and S.-W. Cheong, Nature (London) **429**, 392 (2004).

[12] N. Ikeda, H. Ohsumi, K. Ohwada, K. Ishii, T. Inami, K. Kakurai, Y. Murakami, K. Yoshii, S. Mori, Y. Horibe, and H. Kito, Nature (London) **436**, 1136 (2005).

[13] H. Katsura, N. Nagaosa, and A. V. Balatsky, Phys. Rev. Lett. **95**, 057205 (2005).

[14] M. V. Mostovoy, Phys. Rev. Lett. **96**, 067601 (2006).

[15] Y. J. Choi, H. T. Yi, S. Lee, Q. Huang, V. Kiryukhin, and S.-W. Cheong, Phys. Rev. Lett. **100**, 047601 (2008).

[16] I. A. Sergienko and E. Dagotto, Phys. Rev. B **73**, 094434 (2006).

[17] A. B. Harris, T. Yildirim, A. Aharony, and O. Entin-Wohlman, Phys. Rev. B **73**, 184433 (2006).

[18] T. Basu, V. V. R. Kishore, S. Gohil, K. Singh, N. Mohapatra, S. Bhattacharjee, B. Gonde, N. P. Lalla, P. Mahadevan, S. Ghosh, and E. V. Sampathkumaran, Sci. Rep. **4**, 5636 (2014).

[19] T. Basu, K. K. Iyer, K. Singh, and E. V. Sampathkumaran, Sci. Rep. **3**, 3104 (2013).

[20] Y. J. Shan, Y. Yoshioka, M. Wakeshima, K. Tezuka, and H. Imoto, J. Solid State Chem. **211**, 63 (2014).

[21] Z. Y. Zhao, X. Y. Yue, J. Y. Li, N. Li, H. L. Che, X. F. Sun, and Z. Z. He, Phys. Rev. B **105**, 144406 (2022).

[22] V. Hardy, S. Lambert, M. R. Lees, and D. McK. Paul, Phys. Rev. B **68**, 014424 (2003).

[23] R. Bindu, K. Maiti, S. Khalid, and E. V. Sampathkumaran, Phys. Rev. B **79**, 094103 (2009).

[24] J. Rodríguez-Carvajal, Phys. B: Condens. Matter **192**, 55 (1993).

[25] V. Petříček, M. Dusek, and L. Palatinus, Z. Kristallogr.-Cryst. Mater. B **229**, 345 (2014).

[26] A. Di Cicco, G. Aquilanti, M. Minicucci, E. Principi, N. Novello, A. Cognigni, and L. Olivi, J. Phys.: Conf. Ser. **190**, 012043 (2009).

[27] M. A. Korotin, S. Yu. Ezhov, I. V. Solovyev, V. I. Anisimov, D. I. Khomskii, and G. A. Sawatzky, Phys. Rev. B **54**, 5309 (1996).

[28] Z. W. Li, Y. Drees, C. Y. Kuo, H. Guo, A. Ricci, D. Lamago, O. Sobolev, U. Rütt, O. Gutowski, T. W. Pi, A. Piovano, W. Schmidt, K. Mogare, Z. Hu, L. H. Tjeng, and A. C. Komarek, Sci. Rep. **6**, 25117 (2016).

[29] J. Chen, Y. Chin, M. Valldor, Z. Hu, J. Lee, S. Haw, N. Hiraoka, H. Ishii, C. Pao, K. Tsuei, J. Lee, H. Lin, L. Jang, A. Tanaka, C. Chen, and L. H. Tjeng, J. Am. Chem. Soc. **136**, 1514 (2014).

[30] P. D. Bonnitcha, M. D. Hall, C. K. Underwood, G. J. Foran, M. Zhang, P. J. Beale, and T. W. Hambley, J. Inorg. Biochem. **100**, 963 (2006).

[31] F. de Groot, G. Vankó, and P. Glatzel, J. Phys.: Condens. Matter **21**, 104207 (2009).

[32] B. You, N. Jiang, M. Sheng, S. Gul, J. Yano, and Y. Sun, Chem. Mater. **27**, 7636 (2015).

[33] H. C. Choi, S. Y. Lee, S. B. Kim, M. G. Kim, M. K. Lee, H. J. Shin, and J. S. Lee, J. Phys. Chem. B **106**, 9252 (2002).

[34] J. Zhou, Y. Wang, X. Su, S. Gu, R. Liu, Y. Huang, S. Yan, J. Li, and S. Zhang, Energy Environ. Sci. **12**, 739 (2019).

[35] K. J. Gaskell, A. L. Asunskis, and P. M. A. Sherwood, Surf. Sci. Spectra **9**, 151 (2002).

[36] P. Pal, A. Sahoo, Md. F. Abdullah, S. D. Kaushik, P. N. Vishwakarma, and A. K. Singh, J. Appl. Phys. **124**, 164110 (2018).

[37] A. Bandyopadhyay, S. K. Neogi, A. Paul, C. Meneghini, I. Dasgupta, S. Bandyopadhyay, and S. Ray, Phys. Rev. B **95**, 024432 (2017).

[38] See Supplemental Material at http://link.aps.org/supplemental/10.1103/PhysRevB.107.155105 for the dc susceptibility data at 500 Oe, heat-capacity data, magnetic spin structure, the explanation of electron paramagnetic resonance (EPR) data, extrapolation of the activation energy data, $P - E$ loops, temperature-dependent structural analysis, and calculation of the magnetocaloric effect.

[39] S. Yamashita, Y. Nakazawa, M. Oguni, Y. Oshima, H. Nojiri, Y. Shimizu, K. Miyagawa, and K. Kanoda, Nat. Phys. **4**, 459 (2008).

[40] R. B. Griffiths, Phys. Rev. Lett. **23**, 17 (1969).

[41] A. J. Bray, Phys. Rev. Lett. **59**, 586 (1987).

[42] J. Deisenhofer, D. Braak, H.-A. Krug von Nidda, J. Hemberger, R. M. Eremina, V. A. Ivanshin, A. M. Balbashov, G. Jug, A. Loidl, T. Kimura, and Y. Tokura, Phys. Rev. Lett. **95**, 257202 (2005).

[43] A. Rathi, P. K. Rout, S. Perweena, R. P. Singh, P. D. Babu, A. Guptaa, R. P. Panta, and G. A. Basheed, J. Magn. Magn. Mater. **468**, 230 (2018).

[44] S. Middey, S. Ray, K. Mukherjee, P. L. Paulose, E. V. Sampathkumaran, C. Meneghini, S. D. Kaushik, V. Siruguri, K. Kovnir, and D. D. Sarma, Phys. Rev. B **83**, 144419 (2011).

[45] S. Majumdar, E. V. Sampathkumaran, D. Eckert, A. Handstein, K.-H. Müller, S. R. Saha, H. Sugawara, and H. Sato, J. Phys.: Condens. Matter **11**, L329 (1999).

[46] D. X. Li, S. Nimorib, Y. Shiokawaa, Y. Hagac, E. Yamamotoc, and Y. Onuki, Solid State Commun. **120**, 227 (2001).

[47] R. A. Saha, A. Bandyopadhyay, I. Schiesaro, A. Bera, M. Mondal, C. Meneghini, and S. Ray, Phys. Rev. B **104**, 045149 (2021).

[48] Y. Song-Liu, L. Sheng, C. Heng, S. Jing-Lin, D. Bo, X. Zheng-Cai, and L. Jian-Qing, Chin. Phys. Lett. **21**, 2285 (2004).

[49] A. Abragham and B. Bleaney, *EPR of Transition Ions* (Clarendon Press, Oxford, 1970).

[50] S. Angappane, M. Pattabiraman, G. Rangarajan, K. Sethupathi, B. Varghese, and V. S. Sastry, J. Phys.: Condens. Matter **19**, 036207 (2007).

[51] L. Chen, J. Fan, W. Tong, D. Hu, Y. Ji, J. Liu, L. Zhang, L. Pi, Y. Zhang, and H. Yang, Sci. Rep. **6**, 14 (2016).

[52] J. F. Scott, J. Phys.: Condens. Matter **20**, 021001 (2008).

[53] W. Kleemann, in *Mesoscopic Phenomena in Multifunctional Materials* (Springer Nature Switzerland AG, 2014), Vol. 198.

[54] D. Viehland, S. J. Jang, L. E. Cross, and M. Wuttig, Phys. Rev. B **46**, 8003 (1992).

[55] P. Lunkenheimer, V. Bobnar, A. V. Pronin, A. I. Ritus, A. A. Volkov, and A. Loidl, Phys. Rev. B **66**, 052105 (2002).

[56] R. A. Saha, A. Halder, D. Fu, M. Itoh, T. Saha-Dasgupta, and S. Ray, Inorg. Chem. **60**, 4068 (2021).